

Cover Letter

Learning 3D Mineral Prospectivity from 3D Geological Models with Convolutional Neural Networks: Application to a Structure-controlled Hydrothermal Gold Deposit

Hao Deng, Yang Zheng, Jin Chen*, Shuyan Yu, Keyan Xiao, Xiancheng Mao

Dear Editors-in-Chief,

Please find the enclosed manuscript entitled "Learning 3d mineral prospectivity from 3d geological models with convolutional neural networks: application in a structure-controlled hydrothermal gold deposit" which we are submitting for exclusive consideration for publication in Computers & Geosciences. We confirm that the submission follows all the requirements and includes all the items of the submission checklist.

The manuscript presents a novel 3D prospectivity modeling method based on CNNs, by which we can learn the mineral prospectivity from 3D geological models without using traditional spatial analysis to design prediction variables. We applied the presented method to a structure-controlled hydrothermal gold deposit and prove that our method can effectively improve the 3D prospectivity efficiency and reduce the workload and risk of deep orebody prospecting.

We provide the source codes in a public repository with details listed in the section "Code availability".

Thanks for your consideration.

Sincerely,

Hao Deng,

Yang Zheng,

Jin Chen* (chenjingis@csu.edu.cn),

Shuyan Yu,

Xiancheng Mao

Highlights

Learning 3D Mineral Prospectivity from 3D Geological Models with Convolutional Neural Networks: Application to a Structure-controlled Hydrothermal Gold Deposit

Hao Deng, Yang Zheng, Jin Chen*, Shuyan Yu, Keyan Xiao, Xiancheng Mao

- Highlight 1 A 3D mineral prospectivity modeling method based on convolutional neural networks.
- Highlight 2 Deep learning of 3D mineral prospectivity from the 3D geological models.
- Highlight 3 Reorganizing the unstructured 3D geological models into convolutional neural networks.
- Highlight 4 A 3D prospectivity modeling framework free of hand-designed predictor variables.

Learning 3D Mineral Prospectivity from 3D Geological Models with Convolutional Neural Networks: Application to a Structure-controlled Hydrothermal Gold Deposit

Hao Deng ^a, Yang Zheng ^a, Jin Chen ^{a*}, Shuyan Yu ^a, Keyan Xiao ^b and Xiancheng Mao ^a

^a Key Laboratory of Metallogenic Prediction of Nonferrous Metals and Geological Environment Monitoring (MOE), School of Geosciences and Info-Physics, Central South University, Changsha 410083, China

^b MNR Laboratory of Metallogeny and Mineral Resource Assessment, Institute of Mineral Resources, Chinese Academy of Geological Sciences, Beijing 100037, China

*Corresponding author: chenjingis@csu.edu.cn

ARTICLE INFO

Keywords:

Keyword 1 3D mineral prospectivity mapping

Keyword 2 Convolutional neural networks

Keyword 3 3D geological models

Keyword 4 Gold deposit

Keyword 5 Structure-controlled deposit

Authorship contribution statement

Hao Deng: conceptualization, methodology, software, and writing. Yang Zheng: methodology, software, formal analysis, and writing - original draft. Jin Chen: investigation, and writing - review & editing. Shuyan Yu: formal analysis, and visualization. Keyan Xiao: supervision. Xiancheng Mao: conceptualization, and supervision.

ABSTRACT

The three-dimensional (3D) geological models are the typical and key data source in the 3D mineral prospectivity modeling. Identifying prospectivity-informative predictor variables from the 3D geological models is a challenging and tedious task. Motivated by the ability of convolutional neural networks (CNNs) to learn the intrinsic features, in this paper, we present a novel method that leverages CNNs to learn 3D mineral prospectivity from the 3D geological models. By exploiting the learning ability of CNNs, the presented method allows for disentangling complex correlation to the mineralization and thus opens a door to circumvent the tedious work for designing the predictor variables. Specifically, to explore the unstructured 3D geological models with the CNNs whose input should be structured, we develop a 2D CNN framework in which the geometry of geological boundary is compiled and reorganized into multi-channel images and fed into the CNN. This ensures an effective and efficient training of CNNs while allowing the prospective model to approximate the ore-forming process. The presented method is applied to a typical structure-controlled hydrothermal deposit, the Dayingezhuang gold deposit, eastern China, in which the presented method was compared with the prospectivity modeling methods using hand-designed predictor variables. The results demonstrate the presented method capacitates a performance boost of the 3D prospectivity modeling and empowers us to decrease work-load and prospecting risk in prediction of deep-seated orebodies.

1. Introduction

With the significant advance in 3D GIS and 3D geological modeling techniques, the 3D mineral prospectivity modeling (MPM) has shown its strength in deep prospecting. The 3D MPM, likewise to the 2D MPM, contains three stages necessary towards 3D modeling of exploration target (Carranza, 2011; Porwal and Carranza, 2015): 1) conceptual modeling of the targeted deposits, 2) deriving of appropriate predictor variables, and 3) integration of the predictor variables to output prospectivity. Among these stages, deriving geologically consistent and mineralization-associated predictor variables for each targeting element is the most critical stage in MPM process (Carranza, 2011; Porwal and Carranza, 2015).

In contrast to the 2D MPM, one of the most important data sources for 3D MPM is the 3D geological models. The models of the geological boundaries potentially indicate the areas with high permeability (Snow, 1969; Lisle, 1994; Liu et al., 2012), the locations of fluids conduits (Kyne et al., 2019; Wilson et al., 2016), and the transition zone of physical and chemical properties (Ord et al., 2002; Hu et al., 2020; Cao et al., 2020), where are typically in favor of metal deposition. The 3D geological models have been thought to be the key data source used for deriving predictor variables in 3D MPM (Wang et al., 2011; Nielsen et al., 2015; Xiao et al., 2015). To extract informative predictor variables from the 3D geological models, intensive research efforts have been paid on spatial analysis to the 3D geological models (Li et al., 2015a, 2016; Wang et al., 2015; Mao et al., 2016, 2019; Zhang et al., 2017; Hu et al., 2018; Jin et al., 2020). Generally, extracting mineralization-associated predictor variables from 3D geological models requires considerable domain expertise and a careful trial-and-error process. The extracted predictor variables are subsequently integrated in order to build mineral prospectivity models. Integration of such “hand-crafted” predictor variables, however, can still be limited in the ability to represent the complex controls and the underlying correlation to the mineralization.

Deep learning (LeCun et al., 2015), accompanied by the arrival of the big data era, has dramatically affected many domains (Krizhevsky et al., 2012; Hinton et al., 2012; Jean et al., 2016; Silver et al., 2016; Esteva et al., 2017; Maxmen, 2018; Zuo et al., 2019). Attributed to the ability to automatically learning high-level representation, the deep learning method can discover intricate patterns within the datasets. In the 3D prospecting scenario, the prospecting area is generally experienced tens of years of exploration and mining, which makes it possible to accumulate a large amount

of geological and exploration data to reveal the 3D geological architectures. Given the 3D geological dataset for generating the training data, deep learning is expected to learn a high-level representation that is more associated with mineralization. In this paper, we introduce deep learning into 3D mineral prospecting to circumvent the exhaustive process for “hand-crafting” the predictor variables. While several deep learning methods in 2D mineral prospectivity mapping have been proposed in recent years (Zuo and Xiong 2018; Xiong et al., 2018; Li et al., 2021 Zhang et al., 2021), to the best of our knowledge, our work is the first to offer a deep learning framework for 3D MPM, which hopes to shed new light on the 3D prospecting.

Among the deep learning architectures, convolutional neural networks (CNNs) have achieved extraordinary success due to their shared-weight mechanism of the convolution kernels for feature extraction. To fully explore the spatial correlation within the geological data, in this paper, deep CNNs are adopted to exploit spatial information within the 3D geological models. However, given the 3D geological models, it is nontrivial to build prospectivity models with CNNs. This is because (1) the unstructured 3D geological models cannot be directly input to the CNNs that requires a regular raster input, (2) the entire deep learning framework should be carefully designed to ensure that CNNs can learn the geological control from the geometry of 3D models, and (3) the training of CNNs should be made easy despite the training data is relatively sufficient in 3D MPM.

To achieve prospectivity modeling with CNNs, we reorganize the 3D geological data into 2D multi-channel images for learning the high-level representation from the 3D geological models. This capacitates a detailed geometry representation of the geological boundaries while allowing us to use mature CNNs architecture to build the prospectivity model in an effective and efficient fashion. The prospectivity-informative representation learned with the CNN is then used to outputs a posterior probability of mineralization and finally bridges the gap between 3D geological architectures and mineralization. And we show that the proposed framework allows the prospective model to approximate the ore-forming process. The presented method is applied to the Dayingezhuang orogenic gold deposit, eastern China, in which the detachment fault plays a dominant role in controlling the ore formation. Thus, the Dayingezhuang deposit can serve as an appropriate example to carry out 3D MPM by exploring the geometry of 3D models (Mao et al., 2019) and examining the performance of the proposed method in identifying the mineral prospective areas.

2. Methodology

2.1. Overview

Given the 3D geological models that are a typical unorganized dataset, an intuitive and natural solution, at first glance, is to voxelize the 3D geological space and to construct a 3D CNN that directly works in the voxelized 3D space. While a voxelized 3D geological model seems logical to preserve the original spatial information of the geological bodies, building a 3D CNN would require a large scale of training samples. To train a 3D CNN with limited training samples available in a single study area, we have to severely reduce specified voxel size input to the 3D CNN. Such a compromise would lead to a coarse and sparse representation of shape features or a limited 3D window size, which would in turn lose spatial information related to the shape of geological boundaries.

Instead, we project the 3D shape information onto 2D images and use a 2D CNN to learn the projected images. This allows us to keep a high-resolution representation of the detailed shape of geological boundaries and a smaller training set requirement to train the model. Additionally, the surface distance information is further encoded as a distance channel in the 2D images. Despite such a 2.5D reorganization of 3D data losses some spatial information, for each target voxel, we carefully setting up the projection direction such that the projected image depicts the major shape and configurations of geological boundary that control ore-forming process. Here using the surface distance information also permits us to obtain a large perception range to the metallogenic space. Another advantage of using 2D CNNs is that we can re-purpose the available 2D CNN architectures that have achieved remarkable success in many tasks (Donahue et al., 2014). And the 2D CNNs can benefit from massive pre-training data such as ImageNet to learn generic features about shape and pattern (Kalogerakis et al., 2017). Therefore, we realize the 3D MPM with 2D CNNs, which enables an effective and efficient training of the prospectivity model.

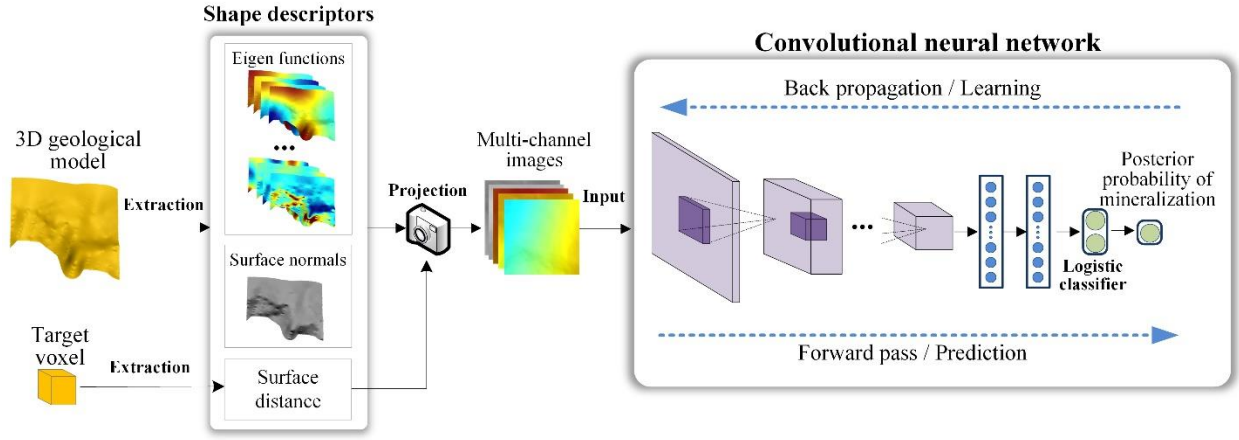


Figure 1: 3D MPM pipeline and architecture that use the 2D CNN to learn from the 3D geological model.

To leverage the 2D CNNs for 3D MPM, we develop a pipeline as shown in Figure 1. Firstly, the original shape of 3D geological models is compiled into several concise but informative shape descriptors (Subsection 2.2). Next, for each target voxel, the extracted shape descriptors are projected into multi-channel images (Subsection 2.3), which, integrated with the surface distance information, encode the shape of 3D geological boundary and the metallogenic control to each target voxel. The projected multi-channel images of target voxels are further fed into the 2D CNN (Subsection 2.4). Taking the input of projected views, 2D CNNs transform the images into compact and robust representations at the top of the networks. The representation is finally incorporated into a logistic classifier that outputs the posterior probability of mineralization for the target voxels. The entire network, from the multi-channel images to the final output, is trained with a backpropagation process. In this manner, the CNN-based pipeline associates the 3D geological models with the ore-bearing probability for the target voxels, resulting in an effective 3D prospectivity model. And we justify the CNN-based framework can be consistent with the ore-forming process (Subsection 2.4).

2.2. Shape descriptors

In 3D space, the surface of a 3D geological model can be represented as embedding manifolds in \mathbb{R}^3 , it is not friendly and adaptive for the input of CNNs. Thus, we compile the geometry of the geological boundaries into several shape descriptors. To fully exploit the available 3D information, we use three types of attributes as the shape descriptors: Laplace Beltrami eigenfunctions, surface normals, and surface distance. The Laplace Beltrami eigenfunctions, as we can see in the following, measure the intrinsic structures in the 3D geometry. The surface normal encodes the local

dip and strike of the surface. Finally, the surface distance represents the proximity from a given voxel to the geological boundaries.

The Laplace Beltrami eigenfunctions are derived from the Laplacian Beltrami operator, which quantifies the global geometry for any given point on the surface. Representing a real function defined on a compact manifold surface M as $f: M \rightarrow \mathbb{R}$, the Laplace Beltrami differential operator Δ over M is defined as the divergence of the gradient:

$$\Delta f = \nabla \cdot (\nabla f), \quad (1)$$

where $\nabla \cdot$ and ∇ denotes the divergence and gradient operator over M , respectively. Since the Laplace-Beltrami operator over M is bounded and symmetric positive semidefinite, the eigendecomposition of Δ can be solved via an eigenproblem over M :

$$\Delta \phi = \lambda \phi. \quad (2)$$

The solution of Equation (2) results in a series of nonnegative eigenvalues $\lambda_i \geq 0$ and the corresponding eigenfunctions ϕ_i . These eigenfunctions are referred to as the Laplace-Beltrami eigenfunctions.

The Laplace-Beltrami eigenfunctions are equivalent to the basis of the Fourier transform on manifold (Taubin et al., 1995). The linear span of the Laplace-Beltrami eigenfunctions forms the spectral domain, which lays the foundation for spectral techniques in geometry processing. We refer the interested readers to Zhang et al. (2010) for more details.

The eigenfunctions have several useful properties, in which the following two are what we are interested in:

1. The eigenfunctions are invariant to isometry deformations and can be used to characterize the intrinsic shape of manifolds in an isometry-invariant fashion.
2. The set of eigenfunctions corresponding to different eigenvalues are orthogonal to each other, forming a complete basis for the L^2 function on the surface. That is, given any square-integrable function f on the surface, we can expand f using the eigenfunctions:

$$f = c_0 \phi_0 + c_1 \phi_1 + \dots, \quad (3)$$

where $c_i = \langle f, \phi_i \rangle = \int_S f \phi_i$ is the coefficient. That is, analogous to the Fourier analysis, f can be represented in the spectral domain expanded by the eigenfunctions.

Regarding the above properties, the Laplace Beltrami eigenfunctions provide a natural and effective tool to preserve the shape information after the projection of 3D geological models, while serving as the basis for approximation of the functions on the surfaces of 3D geological models.

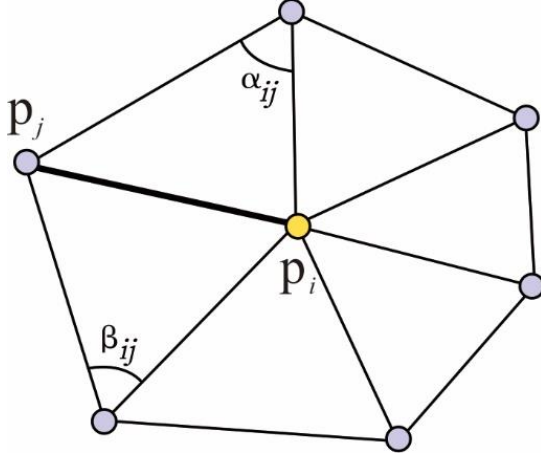


Figure 2: Laplacian operator.

To calculate the Laplace Beltrami eigenfunctions for 3D geological models, we define the Laplace Beltrami operator in a discrete form. Following the approach (Meyer et al., 2003), the discrete Laplace–Beltrami operator Δf over the i -th vertex p_i can be approximated as:

$$\Delta f(p_i) \approx \frac{1}{s_i} \sum_{j \in N(i)} \frac{\cot \alpha_{ij} + \cot \beta_{ij}}{2} (f(p_j) - f(p_i)) = \frac{1}{s_i} \sum_{j \in N(i)} m_{ij} (f(p_j) - f(p_i)), \quad (4)$$

where $N(i)$ denotes the indices for the set of the adjacent vertex of the p_i , s_i is the area of Voronoi region of p_i , the angles α_{ij} and β_{ij} are illustrated in Figure 2, and $m_{ij} = \frac{\cot \alpha_{ij} + \cot \beta_{ij}}{2}$. By representing the eigenfunction values at n vertices of the 3D geological model as an n -order vector \mathbf{f} , in terms of Equation (4), the Laplace–Beltrami operator Δf over the triangular mesh can be written as $\Delta \mathbf{f} = \mathbf{L} \mathbf{f}$. Here \mathbf{L} is the Laplacian matrix whose entries is defined as:

$$\mathbf{L}_{ij} = \begin{cases} -\sum_k m_{ik}/s_i, & \text{if } i = j, \\ \frac{m_{ij}}{s_i}, & \text{if } i \text{ and } j \text{ adjacent,} \\ 0, & \text{otherwise.} \end{cases} \quad (5)$$

The eigendecomposition of the discrete Laplace–Beltrami operator can be calculated by the eigendecomposition of \mathbf{L} :

$$\mathbf{L} = \mathbf{\Phi} \mathbf{\Lambda} \mathbf{\Phi}^T \quad (6)$$

where $\mathbf{\Lambda}$ is the diagonal matrix of eigenvalues of \mathbf{L} , and $\mathbf{\Phi}$ is the matrix of eigenvectors. In this manner, we obtain discrete Laplace–Beltrami eigenvectors as the intrinsic shape descriptor for the 3D geological models.

2.3. Shape projection

In order to input the shape descriptors of 3D models into CNNs, we reorganize the shape descriptors into images. Here the perspective projection is leveraged to reorganize the shape descriptors into multi-channel images, in which each channel corresponds to a single descriptor. Given a target voxel, such a projection process generates the projected images that illustrate the shape of the geological boundary viewed from the target voxel. In other words, the projection of shape descriptors into images implicitly encodes and represents the metallogenic controls to the target voxel.

To facilitate the CNNs to learn the association between the shape descriptors and the mineralization, we wish to enforce the projected images to capture the key control areas of the geological boundary. The results of the projected images depend on the viewing direction from the target voxel. Thus, capturing the key control area of the geological boundary can be cast to a viewing direction searching problem. That is to search for a viewing direction \mathbf{d} such that the major control areas of the geological boundary can be projected as much as possible.

For a target voxel denoted by its center point \mathbf{v} and its controlling geological boundary denoted by its surface S , if we project S through the viewing direction \mathbf{d} , the metallogenic control $C(\mathbf{d})$ from the projected areas of S in the resulting image can be measured as:

$$C(\mathbf{d}) = \int_{\text{projected}(\mathbf{d}, \mathbf{v}) \in S} C(\mathbf{x}, \mathbf{v}) d\mathbf{x}, \quad (7)$$

where $\text{projected}(\mathbf{d}, \mathbf{v}) \in S$ denotes the projected area of S using viewing direction \mathbf{d} at viewing position \mathbf{v} , and $C(\mathbf{x}, \mathbf{v})$ denotes the metallogenic control from a point \mathbf{x} on S to \mathbf{v} . Thereby, searing for an optimized viewing direction \mathbf{d}^* can be optimized by maximizing Equation (7):

$$\mathbf{d}^* = \arg \max_{\mathbf{d}} C(\mathbf{d}). \quad (8)$$

Given the optimization problem in Equation (8), using general optimization techniques such as gradient descend is intractable. Inspired by the mean-shift algorithm, instead, we design an algorithm to achieve the optimization. Initially, we calculate the closest point \mathbf{c}_0 on S to \mathbf{v} , and set the \mathbf{d} towards \mathbf{c}_0 . Using this setting, we generate the projected

image of S . Then we calculated the centroid of the image for shifting the viewing direction so as to maximize Equation (7). For all image coordinates $\{u_i\}_{i=1}^m$ corresponds to the projection of S in the image, the centroid u of the image is calculated as:

$$u = \frac{\sum_{i=1}^m u_i C(\mathbf{x}_i, \mathbf{v})}{\sum_{i=1}^m C(\mathbf{x}_i, \mathbf{v})}, \quad (9)$$

where $\mathbf{x}_i \in S$ is the corresponding point on S projected to u_i . After obtaining the centroid u , we unproject it to find the corresponding point \mathbf{c} on S and shift the viewing towards \mathbf{c} to generate a new projected image. The above shift-and-projection process is repeated iteratively until the convergence of the viewing direction. Considering the control from the geological boundary is closely related to the proximity to the geological boundary, in our implementation, we set $C(\mathbf{x}, \mathbf{v}) = \frac{1}{r}$, where $r = \|\mathbf{x} - \mathbf{v}\|$. And our numeric test found that the optimization process converges less than 20 iterations (Figure 3).

We generate the projected images using graphical rendering. Given the viewing direction, we render the 3D geological models from the viewpoint to output the projected images. Here the viewing position \mathbf{p} for the projection is placed according to the location \mathbf{v} of the target voxel and the viewing direction φ . This is calculated by shifting \mathbf{v} backward along with \mathbf{d} : $\mathbf{p} = \mathbf{v} - t\mathbf{d}$, where t is the shifting distance. We set $t = 1000\text{m}$ in our implementation to allow the projected image to cover large areas of the geological boundary. During the rendering, the values of shape descriptors are interpolated and assigned to the projected pixels by using the rasterization pipeline of the graphical processing unit (GPU). The parallel rasterization pipeline of GPUs enables an efficient performance of the projection. A side benefit of using GPU is a fast calculation of the surface distance. When the 3D geological model is rendered, the depth values are obtained as a by-product of the depth test in the rasterization pipeline, which can be converted into the surface distance efficiently. Thus, the overall projection process can be performed efficiently, which finally generates massive multi-channel images fed into CNNs.

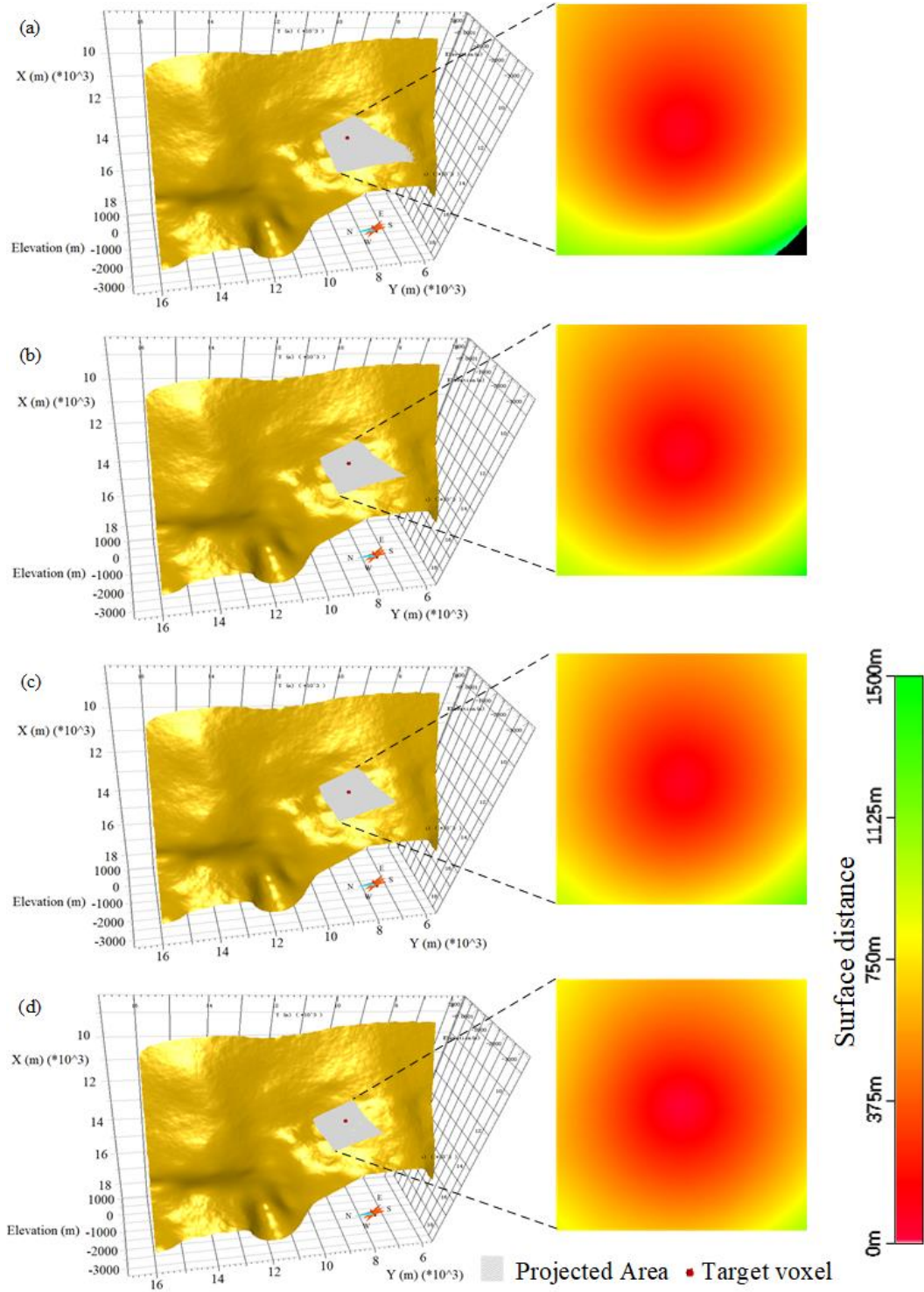


Figure 3: The iteration process in optimization of the viewing direction: the projected areas (left column) and the projected images illustrating the distance to the target voxel (right column) at (a) 1st, (b) 3rd, (c) 4th and (d) 11th iterations are presented. Note that the projected areas gradually converge to the zone that is more close to the target voxel as the result of maximization of Equation (7).

2.4. Convolutional Neural Networks

CNNs are a type of deep neural networks containing the building blocks of convolutional layers, pooling layers and fully connected layers. By combining the strength of these layers, it results in a deep architecture to capture underlying factors and patterns inside the input data. In an attempt to capture the features informative to the deep mineralization, we leverage a mature architecture of AlexNet (Krizhevsky et al., 2012), a significant milestone of CNNs, as the backbone for learning of high-level representation from the input images. The learned high-level representation is subsequently input to the head architecture of the networks.

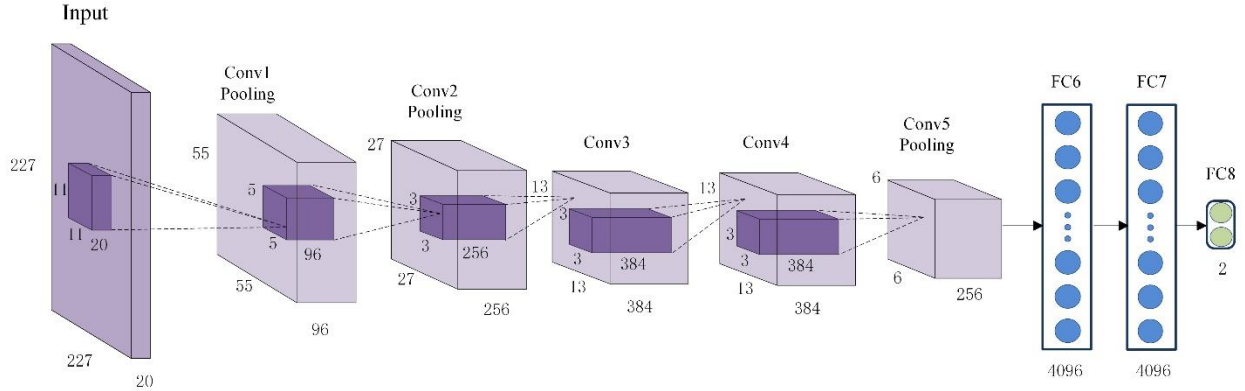


Figure 4: The AlexNet-based CNN architecture for propsectivity modeling.

As shown in figure 4, our AlexNet-based CNN architecture is composed of convolutional layers (Conv1 to Conv5) and fully-connected layers (FC6-FC8) from bottom to top. The convolutional layers apply learned convolutional kernels to the input features (images) to extract a more abstract representation. The stacking of convolutional layers in CNNs allows to gradually extract high-level representations of the input images. Each convolution layer works using a set of convolutional operators and a ReLU nonlinear mapping as the activation operation (Hinton et al., 2010):

$$f_{\theta}(X_i) = \max(0, \mathbf{W}_{i-1} * X_{i-1} + \mathbf{b}_i), \quad (10)$$

where \mathbf{W}_{i-1} denotes the convolutional kernel, $*$ denotes the convolutional operator, and \mathbf{b}_i is the bias. The pooling layers are set up after convolutional layers Conv1, Conv2 and Conv5. The output of Conv5 is input to three fully-connected layers for extracting the final high-level representations.

Different from AlexNet that is originally tailored to the classification of RGB images, our CNN architecture is modified to adapt the data organization and task setting for 3D MPM. Firstly, since the shape of our multi-channel

images is different from the original setting of AlexNet, we modify the size of convolutional kernels at conv1 from $5 \times 5 \times 3$ to $5 \times 56 \times 20$ in order to fit our input. Moreover, the original head architecture is a 1000-class softmax classifier. We replace it with a logistic classifier that outputs the posterior probability of mineralization.

Given the modified CNN architecture, we train it for 3D MPM by using the information of n known voxels. Each voxel, in addition to the associated multi-channel image, is assigned a label y_i with 1 representing ore-bearing or 0 otherwise. We train the parameters θ of the CNN model $f_\theta(X)$ by minimizing the objective function $L(\theta)$. The objective function has two terms: a cross-entropy loss for guiding the CNNs to fit the training data and a regularization term for preventing $f_\theta(X)$ from overfitting the training data. The final objective function $L(\theta)$ is formulated as:

$$L(\theta) = - \sum_{i=1}^n (y_i \log f_\theta(X_i) + (1 - y_i) \log(1 - f_\theta(X_i))) + \lambda \|\theta\|^2, \quad (11)$$

where the first term is cross-entropy loss and the other one is the regularized term, and λ denotes a weighting to balance the two terms. Using the derivative of Equation (11), we can train the CNN with backpropagation.

2.5. Justification

Our CNN-based framework for 3D MPM can be interpreted from a perspective of ore-forming dynamics. The key governing equation for the hydrothermal process is the convection-diffusion-reaction equation, which describes the heat transfer, mass transport and chemical reactions in the ore-forming process. The steady-state convection-diffusion-reaction equation for ore systems (Zhao et al., 2008) is formulated as:

$$\nabla \cdot (D \nabla C) - \nabla \cdot (Cq) + KC + F = 0, \quad (12)$$

where C is the concentration (for mass transfer scenario) or temperature (for heat transfer scenario) at position x and time t , D is the diffusivity, q is the Darcy velocity, K is the first-order reaction velocity, and F is source function.

Applying the Green's function method, the solution of Equation (12) has the form:

$$C(x) = \iiint_V G(x, y) F(y) dV, \quad (13)$$

where $G(x, y)$ is the Green's function for the partial differential equation problem in Equation (13).

Using the divergence theorem, Equation (13) is transformed to

$$C(x) = \iint_S H(x, y) \cdot \mathbf{n} dS, \quad (14)$$

where $H(x, y) = \frac{1}{4\pi} \iiint_V G(x, z) F(z) \frac{y-z}{\|y-z\|^3} dV$, \mathbf{n} is the surface normal.

Equation (14) demonstrates that the spatial distribution of mass and heat can be expressed in a form of surface integral over the boundary of the mass source and/or heat source. In this regard, our projection process is analogous to converting the 3D scenario to 2D one from Equation (13) to Equation (14). Specifically, the CNN can be considered as an approximation to the surface integral over the geological boundary in Equation (14), which learns to “integrate” over the projection areas of the geological boundary. Note that the multi-channel images include the channels of Laplace-Beltrami eigenfunctions, the linear combination of which are capable of approximating arbitrary square-integrable function f on the surface. Thus, channels of Laplace-Beltrami eigenfunctions can serve as the basis for modeling the surface function like $H(x, y)$ in Equation (14). Additionally, the channels of surface normals and surface distance describe the shape of the surface, which can facilitate the approximation to the surface integral in Equation (14). Thereby, when feeding the multi-channel images and the associated mineralization information into the CNN, the CNN is allowed to learn the representation related to the hydrothermal transport process. Attribute to the learning and representation capability of the CNN, the CNN is further expected to disentangle the underlying correlation to the mineral deposition that is closely related to the geometry of the geological boundary. In summary, the setting of our deep learning framework facilitates the learning of a mapping from the shape of geological boundaries to the localization of mineralization.

3. Study area

The Jiaodong Peninsula is located in the eastern North China Craton and has been documented as the largest gold province in China with more than 4500 t gold reserves. The large-scale Dayingezhuang Au deposit (> 130 t) is sited in the middle segment of the Zhaoping fault, northwestern Jiaodong Peninsula (Figure 5). It is principally hosted in Zhaoping fault, which exhibits the metamorphosed Archean Jiaodong Group as the hanging wall and the Jurassic Linglong granite as the footwall of the Zhaoping fault (Figure 6). The Jiaodong Group was metamorphosed into the amphibolite and granulite facies and is mainly composed of amphibolites, granulites, and gneiss. The Linglong granite is formed as the partial melting of the Jiaodong Group rocks during late Jurassic.

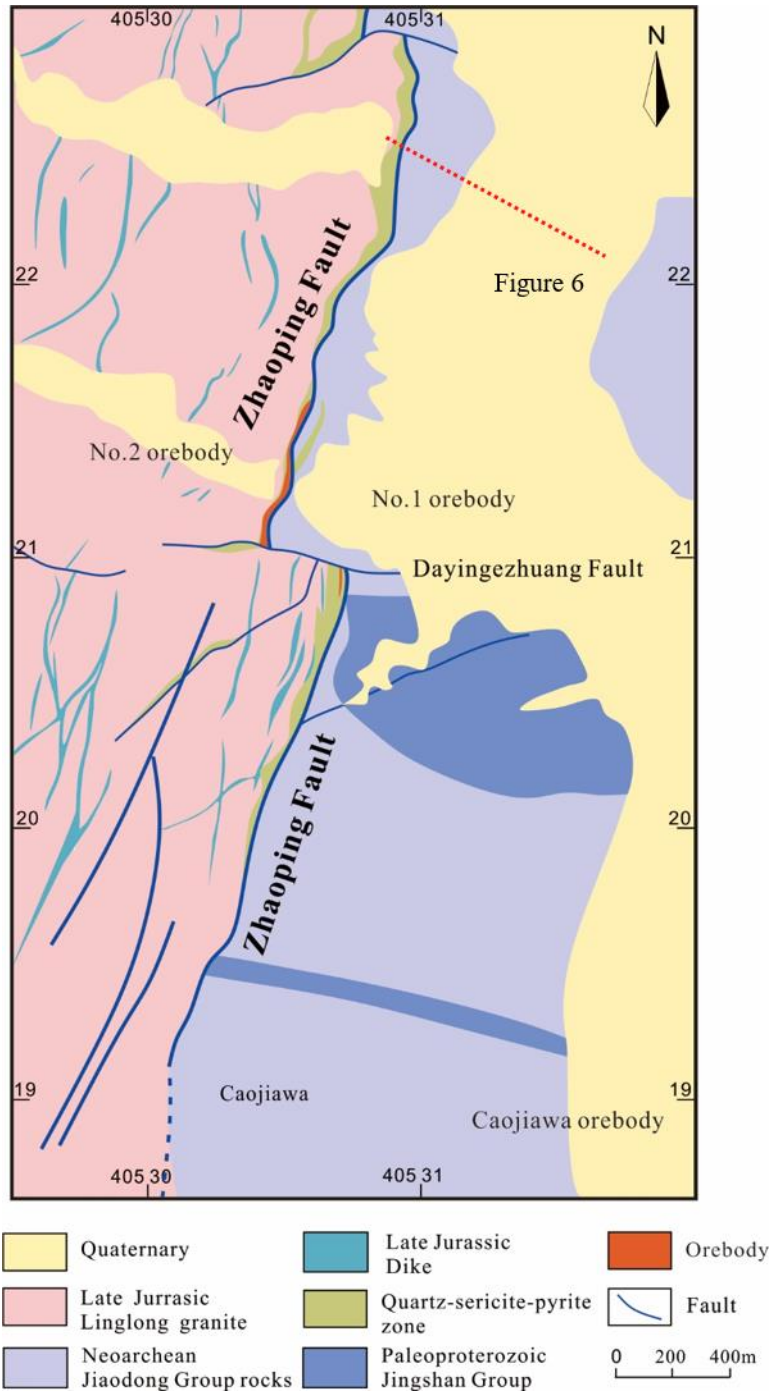


Figure 5: Geological map of the Dayingezhuang gold deposit (after Mao et al., 2019).

The Zhaoping detachment fault, developed along with the interface between the Jiaodong Group rocks and the Linglong granite, generally strikes SW–NE with SE dips of 35°–60° (Mao et al., 2019). It shows a gentle shape undulation both along the strike and dip directions. The fault zone is comprised of mylonitic–ultramylonitic rocks and

irregular breccias and is characterized by a ductile-brittle to brittle deformation properties. During the mineralizing period, the Zhaoping fault underwent a dextral strike-slip normal sense of deformation in NW–SE-striking extensional regime. Several secondary faults, e.g., Nanzhoujia, Dayingezhuang, and Nangou, as the post-ore faults, offset the Zhaoping fault and/or the gold orebodies at Dayingezhuang (Figure 5).

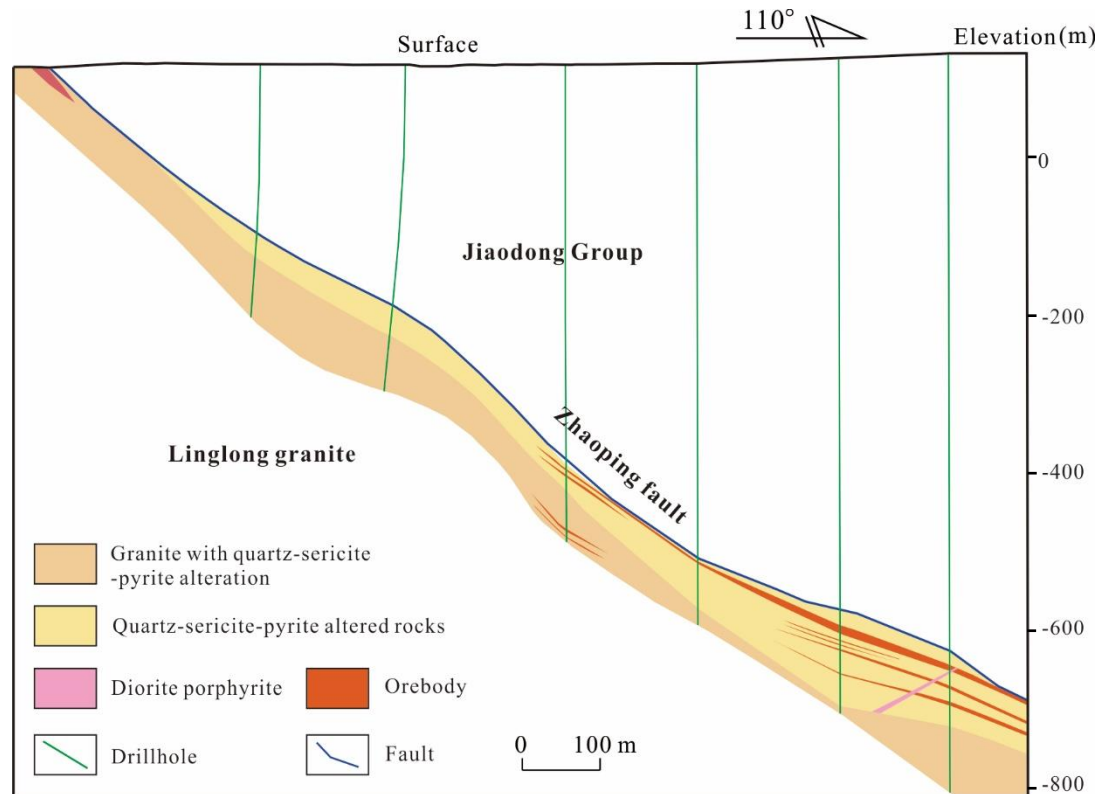


Figure 6: The mineralization-alteration zoning pattern (at section line #86) of the Dayingezhuang gold deposit.

The localization of gold orebodies in Dayingezhuang is closely associated with the Zhaoping fault, which coincides with the geometry of the Zhaoping fault. Most Au mineralization is hosted in the mylonization and brecciation zones in the footwall of the Zhaoping fault. There are major three orebodies, i.e., No. 1, No. 2 and Caojiawa orebodies, in the Dayingezhuang deposit. The No. 2 orebody, with Au grades typically < 5 g/t, contains 65% Au resource in the deposit. It extends along the strike more than 3000 m and 1500 m NE-plunging to deep and exhibits disseminated mineralization and intense quartz-sericite-pyrite alteration. The No. 1 orebody is located in the south segment of the Dayingezhuang deposit and extends about 1500 m along the strike, which consists of disseminated ores and vein ores. The Au grade of No. 1 orebody ranges from 2–4 g/t. The Caojiawa orebody is located to the south of the No. 1 orebody

and extends about –900m, with Au grades < 2 g/t. It is also characterized by the disseminated mineralization associated with quartz-sericite-pyrite alteration and structural deformation.

Previous studies have demonstrated the Dayingezhuang gold deposits and other gold deposits (e.g., Jiaojia and Sanshandao) in the Jiaodong Peninsula could be classified as the atypical orogenic deposits, i.e., Jiaodong-type gold deposits (Goldfarb and Santosh, 2014; Yang et al., 2014, 2016; Song et al., 2015; Deng et al., 2020; Liu et al., 2021a). These gold deposits have similar structural controls on mineralization and ore-forming conditions (the moderate temperature and salinity and the CO₂-rich fluids) but distinct tectonic settings of lithospheric thinning and extension. The gold mineralization is closely associated with the regional detachment faults (e.g., dip and geometry) but not associated with the host rocks or any exposed intrusion (Goldfarb and Santosh, 2014; Li et al., 2015; Mao et al., 2019). The significant structural controls on mineralization essentially results from the influence on rock permeability from structural deformation, driving fluid flows, trapping ore-forming fluids, and/or metal deposition under a fluctuating pressure condition in fault zones (Yang et al., 2016, 2018; Mao et al., 2019; Wang et al., 2019; Liu et al., 2021b). Owing to the dominated controls on ore formation from the detachment faults, the location of gold mineralization at Dayingezhuang could be well inferred from the shape of Zhaoping faults (Mao et al., 2019).

4. Results

4.1. 3D MPM with convolutional networks

To carry out perspective modeling, the current and legacy mine dataset was collected, which contains one 1:10,000 surface geological map, 67 1:500 and 1:1000 subsurface horizontal sections, 58 cross-sections, 95 drillholes, 56 tunnels, 38,198 gold assays (ore and non-ore), and 13 magnetotelluric (MT) sounding profiles (until June 2019). Firstly, the 3D geological models of the Dayingezhuang deposit were constructed according to the exploration data. Since the Zhaoping fault is the major ore-controlling structure, the shape of Zhaoping fault is delineated following the 76 drillholes and 58 cross-sections. For the areas where the exploration data is scarce and missing, we carefully inferred and delineated the location of Zhaoping fault according to MT profiles (Mao et al., 2019). With these delineated contours as constraints, we used the implicit modeling method (Macedo et al., 2011) to interpolate the geometry between the adjacent contours, which results in the fairing implicit function while being faithful to the input delineated

contours. Finally, the 3D mesh model of the Zhaoping fault was generated from the implicit surface. Figure 7(a) illustrates the resulting 3D mesh model of the Zhaoping fault.

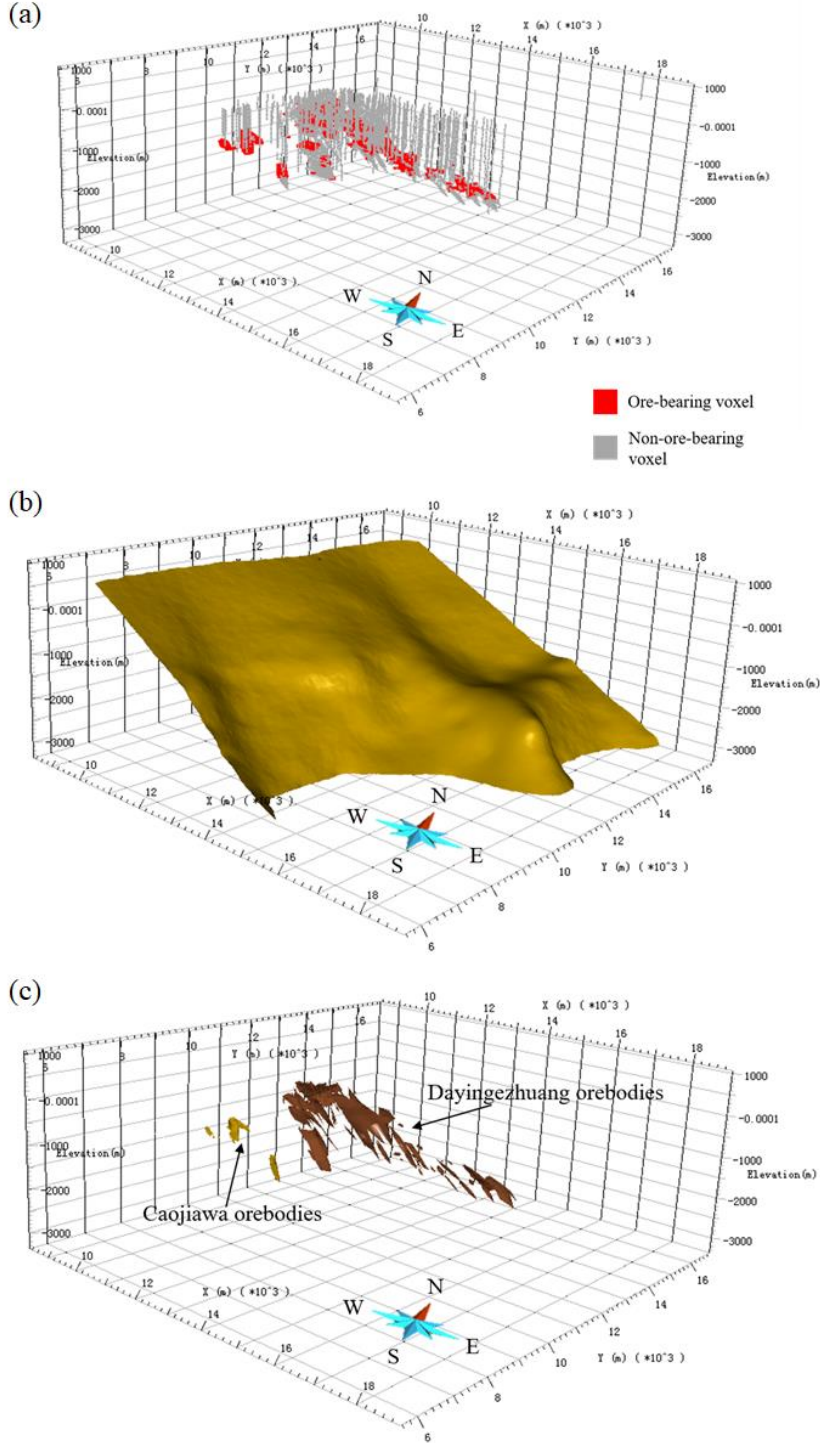


Figure 7: Known voxels (Au grade >1g/t) (a), 3D mesh models of the Zhaoping fault (b) and orebodies (c).

To represent the 3D distribution of mineralization, the 3D mesh models of orebodies were also constructed from the exploration data (Figure 7(b)). On this basis, the voxel models representing Au distribution were built associated with the 3D mesh model of orebodies. The 3D space of Dayingezhuang deposits was divided into voxels each of which has the size of $25\text{m} \times 25\text{m} \times 25\text{m}$. To estimate the Au distribution, the 3D Kriging interpolation was utilized to interpolate the gold concentration for these voxels in terms of 11,488 Au assay samples from the drill-hole data. According to the cut-off grade (1.0g/t) of gold, a total of 4,997 voxels (Figure 7(c)) were labeled as ore-bearing, while leaving the remaining 21,943 voxels labeled as non-ore-bearing.

Given the 3D model of Zhaoping fault, we calculate the shape descriptors of the model. For generating the shape descriptors for the model, we used the first 16 Laplace Beltrami eigenfunctions with non-zero eigenvalues to encode the intrinsic shape of Zhaoping fault, which, in addition to the surface normal, finally forms 19-dimensional shape descriptors for any point of the 3D model. Figure (Figure 8) visualizes the shape descriptors for the Zhaoping fault. To generate the training and testing data, for each voxel, a multi-channel image (Figure 9) was projected at a fixed resolution of $227 \times 227 \times 20$, where the last dimension 20 is the number of channels. That is, 19 channels for shape descriptors and the last one for surface distance in term of the target voxel. In the network training, a ratio of 8:2 was used to partition known voxels into the training set and the validation set.

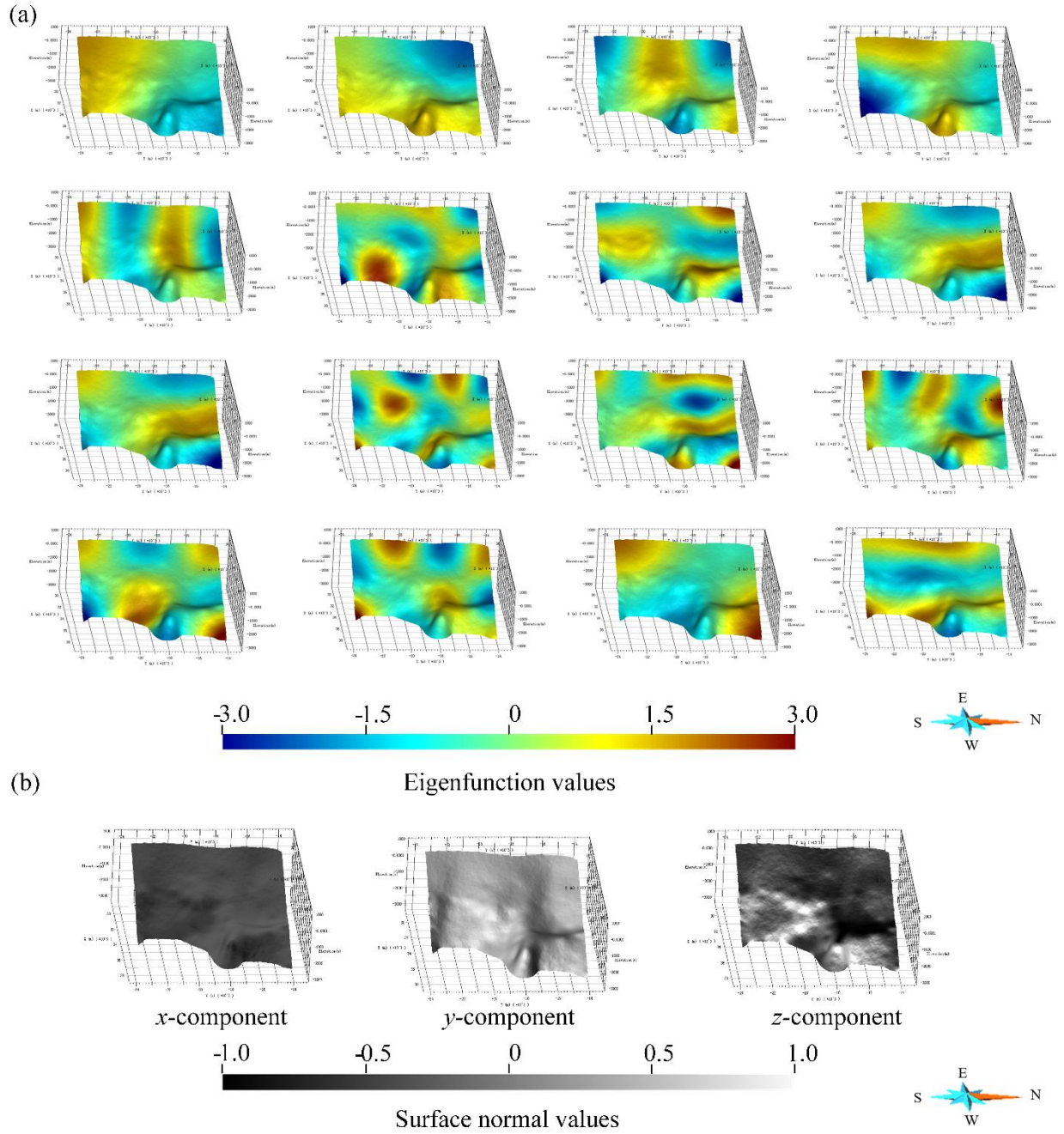


Figure 8: Shape descriptors of (a) eigenfunctions and (b) surface normals of Zhaoping fault, Dayingezhuang segment.

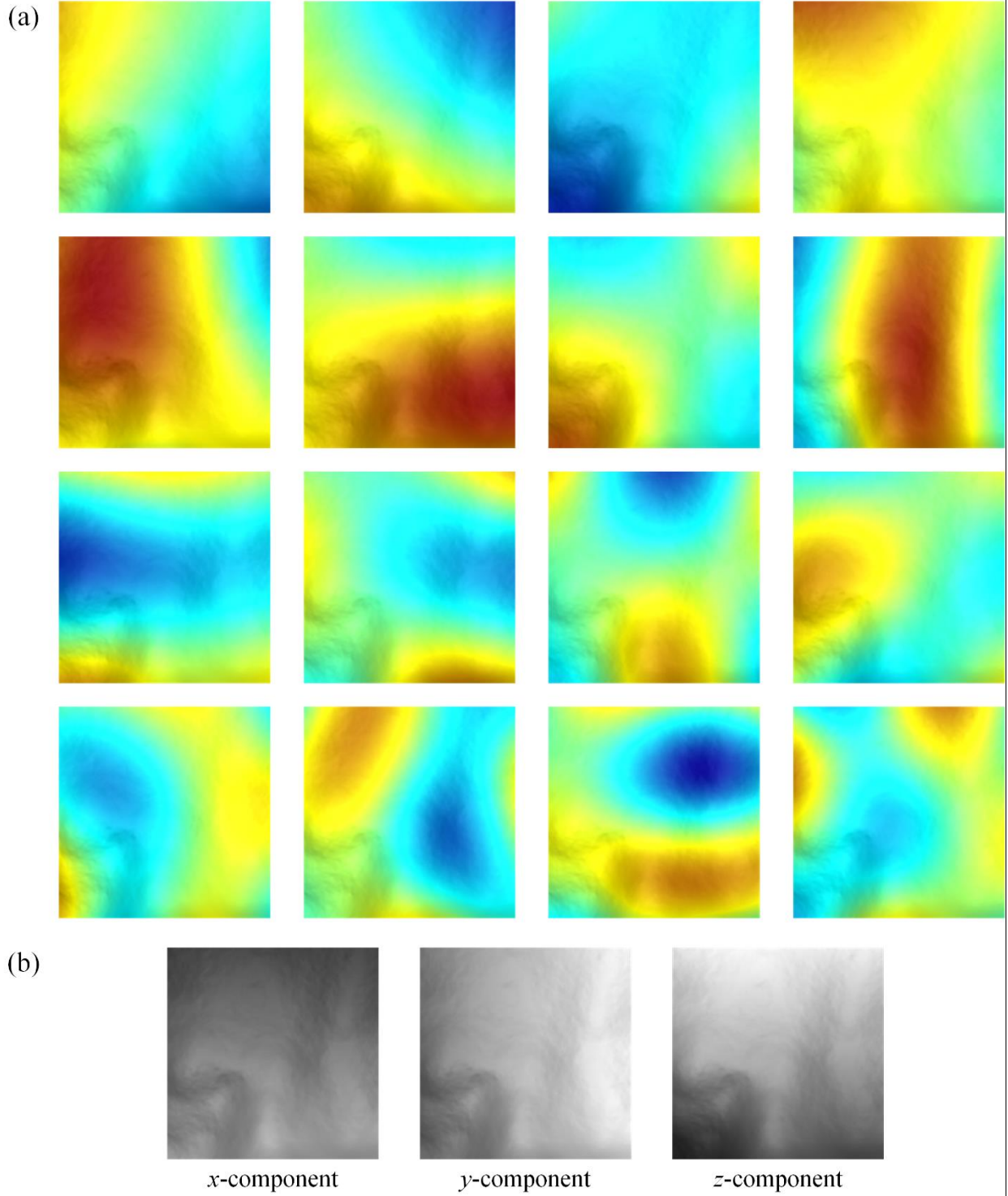


Figure 9: Projected results of shape descriptors: (a) eigenfunctions and (b) surface normals of Zhaoping fault, Dayingezhuang segment (at one location, Size: 227x227).

We implemented our model with TensorFlow (Abadi et al., 2016), an open-source machine learning library developed by the Google Brain. To avoid over-fitting to the training set, we adopt a supervised pre-training scheme to initialize the parameters of the network. Here the deep network is pre-trained with ImageNet (Deng et al., 2009) a large-scale repository, which enables the convolutional filters to capture the shape information in images. After the pre-training process, the network model was trained in a fully supervised fashion by fine-tuning from the pre-trained model.

In the training process, the top convolutional layer and three fully-connected layers, i.e., Conv1, FC6, FC7 and FC8 were not loaded from the pre-trained weights but initialized from scratch using the He initialization strategy (He et al., 2015). The dropout regularization technique (Hinton et al., 2012; Srivastava et al., 2014) was applied during the training. The early stopping solution was used to interrupt the training when the performance on the validation set starts dropping. In the implementation, we took 50 epochs to fully converge, spending about 2 days on one Nvidia RTX 2080Ti 11GB graphics card.

Figure 10 shows the performance of the training set and validation set during training process. It is noted that during training process, the validation accuracy (training loss) increases (decreases) progressively for both the training and validation set. We further verify how the training process impacts the predicted prospectivity of the unknown areas in the Dayingezhuang deposit. The fuzziness, according to the fuzzy set theory (Zadeh, 1965), of the predicted posterior probability at different epochs was used to measure the performance of CNNs in the unknown area. Given the posterior probability $\{p_1^{(t)}, \dots, p_n^{(t)}\}$ for n voxels predicted by CNN trained after t epochs, the fuzziness can be measured as:

$$H(t) = -\frac{1}{n} \sum_{i=1}^n p_i^{(t)} \log p_i^{(t)} + (1 - p_i^{(t)}) \log(1 - p_i^{(t)}). \quad (14)$$

Figure 11 shows the changes of the fuzziness of posterior probability with respect to the different epochs of training. Overall, the above results demonstrate that the CNNs model is effective to identify the association between the shape of the geological model and the ore-bearing information while trained to be more definite to target deep-seated prospectivity areas.

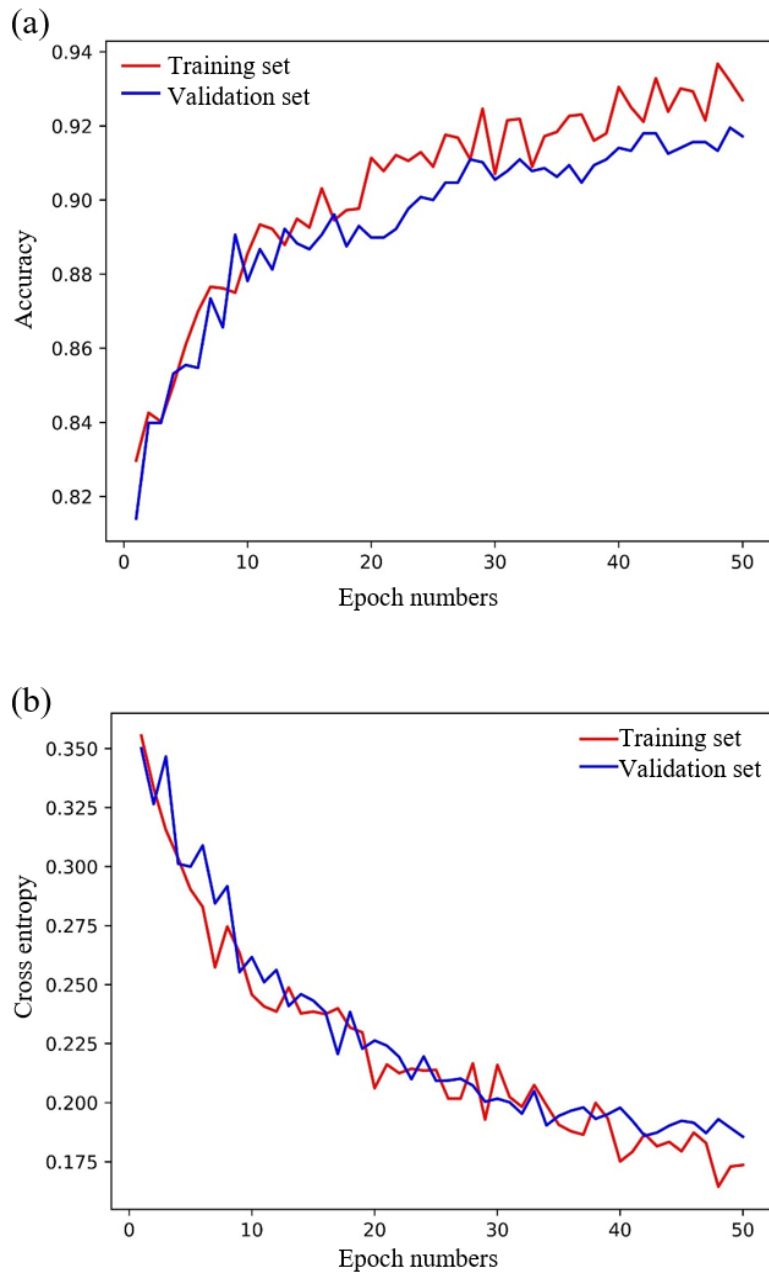


Figure 10: The training procedure for prospectivity modeling (a) accuracy and (b) cross-entropy at different epochs.

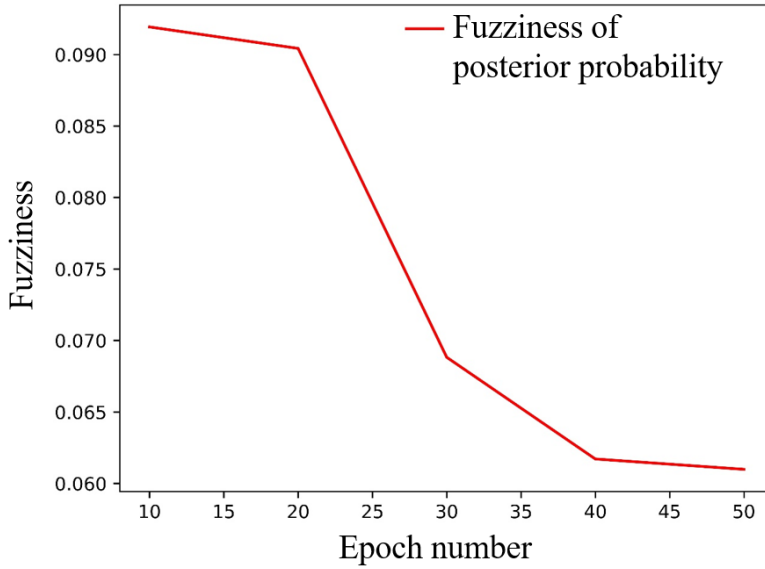


Figure 11: Fuzziness of predicted posterior probability at different epochs.

4.2. 3D MPM based on hand-crafted predictor variables

In order to validate the superiority of our 3D MPM method based on CNNs, we compared our method with the conventional MPM method by using hand-crafted predictor variables. Here the hand-crafted predictor variables are the same as those in (Mao et al., 2019). Table 1 summarizes the predictor variables.

Table 1: Targeting criteria, predictor variables and corresponding spatial analysis approach for 3D MPM in Dayingezhuang deposit.

Targeting criteria	Predictor variable	Spatial analysis approach
Proximity to Zhaoping fault	Euclidian distance to Zhaoping fault	3D Euclidean distance transform
Shape undulation of Zhaoping fault	1st-order / 2nd-order undulation of Zhaoping fault	3D morphological undulation analysis
The dipping of Zhaoping fault	Slope of Zhaoping fault	Slope analysis
Fault shape transition	Dipping variation of Zhaoping fault	3D Geometry transition extraction
Hydrothermal alteration intensity	Thickness of Alteration zone	Field analysis of alteration zone

We computed the predictor variables listed in Table 1 for each voxel. The mineral prospectivity models were constructed by integrating the predictor variables using nonlinear classifiers. To avoid the limitation of the selected classifier and to guarantee the performance of the prospectivity model, we tested a variety of classifiers, including logistic regression (LR) (Agterberg et al., 1993; Bai et al., 2011), support vector machine (SVM) (Shabankareh et al., 2016; Zuo et al., 2011), Random Forests (RF) (Gao et al., 2016) and multi-layer perceptron (MLP) (Baykan et al., 2011; Kumar et al., 2011). To learn the prospectivity model with the above classifiers, the voxels are also partitioned into the training and validation set the same as the partition described in 4.1. Overall, four prospectivity models using hand-crafted predictor variables result from different classifiers.

4.3. Performance evaluation

We compared the proposed method with the aforementioned machine learning methods using hand-crafted predictor variables. To evaluate the performance of these methods, the receiver operating characteristic (ROC) curves (Barreno et al., 2007) and capture-efficiency curves (Agterberg and Bonham-Carter, 2005) were utilized.

The ROC curves are generated by plotting the true positive rate (TPR) against the false positive rate (FPR) at different thresholds for determining the high-prospectivity areas. The area under the curve (AUC) is used to evaluate the ROC curves. The AUC values range from 0.5 to 1. A higher AUC means a better performance of the prospectivity model. In our experiment, the voxels in the validation set were employed to plot the ROC curves. Figure 12(a) illustrates the ROC curves for the prospectivity models obtained by the five MPM methods. It is observed that the ROC curve of the CNN-based model is obviously steeper toward the upper left corner than those of the other four models, which results in an AUC value of 0.96, the highest among the five evaluated prospectivity models. This demonstrates that the CNN-based model outperforms the other four models in 3D MPM.

On the other hand, the capture-efficiency curves were generated by calculating the percentage of ore-bearing voxels against all predicted voxels under the different thresholds. In 3D scenario, a higher success rate means orebodies can be targeted with smaller prospective volumes. Thus, the capture-efficiency curves reflects the efficiency of the prospectivity models, which is a significant criterion for estimating the risky in mineral exploration targeting. Figure 12(b) depicts the capture-efficiency curves of the five prospectivity models. The prospective volume of CNN-based

models to identify known ore-bearing voxels is remarkably lower than those of the other models, while the models using hand-crafted variables require larger volumes to delineate similar percentages of ore-bearing voxels. Thus, the capture-efficiency curves demonstrate the CNN-based model has higher targeting efficiency in identifying high-prospectivity areas compared with those models using hand-crafted predictor variables.

4.4. 3D predictive mapping and target appraisal

The high-prospective areas can be identified as potential areas for future mineral exploration. The maximum Youden index (MYI) (Ruopp et al., 2008) was used to select an optimum threshold of probability for separating the high-prospective areas from the low-prospective background. We compared the high-prospective areas resulting from CNN with those from the random forest, which has the highest AUC among the four competing prospectivity models. Table 2 lists the MYIs and the corresponding probabilities obtaining the MYIs for the CNN and the random forest. It is noted that both the two probabilities are larger than the prior probability of ore-bearing voxels. Figure 13(b) shows the high-prospective areas resulting from the CNN and the random forests model. The high-prospectivity areas resulting from the CNN focus on several potential exploration targets. Most of these high-prospectivity areas overlap the high-prospective areas from the random forest, which reflects the effectiveness of the CNN-based model in identifying high-prospective areas without given the prediction variables. In comparison, the high-prospective areas from the random forest cover more prospecting areas and are less discriminative to target the mineral potential areas.

According to the posterior probability resulting from the CNN-based model, five targets are delineated in the deep-seated areas of Dayingezhuang deposit. There targets I and III extend from the middle of the No. 2 orebodies at average of -1700 m and -1500 m elevations, respectively, which are considered to be the two horizontal branches of the No. 2 orebodies. The target II is located at the deep areas between -1500 m to -1600 m levels at Caojiawa segment, which is general associated with the deep branches of Caojiawa orebodies and shows a NE-SW trend enrichment zones. The target IV is sited on the NE trending direction of No. 2 orebodies at depths from -1800m to -2000m, which is likely the deep extension of the No. 2 orebodies. The target V is located in SSW of No. 2 orebodies at depths from -1900 m to -2300 m, which has a lower posterior probability compared with the above four targets.

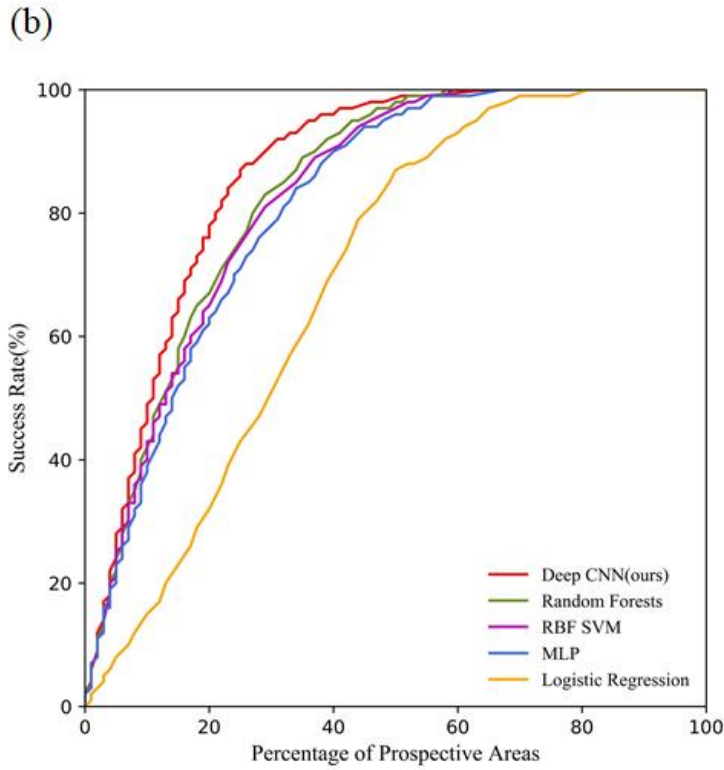
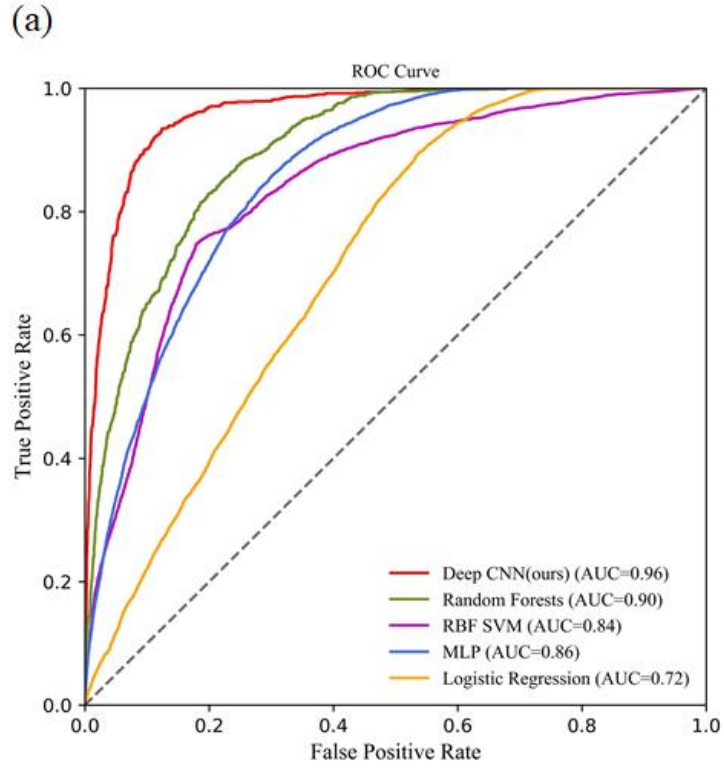


Figure 12: ROC curves (a) and capture-efficiency curves (b) of five evaluated prospectivity models.

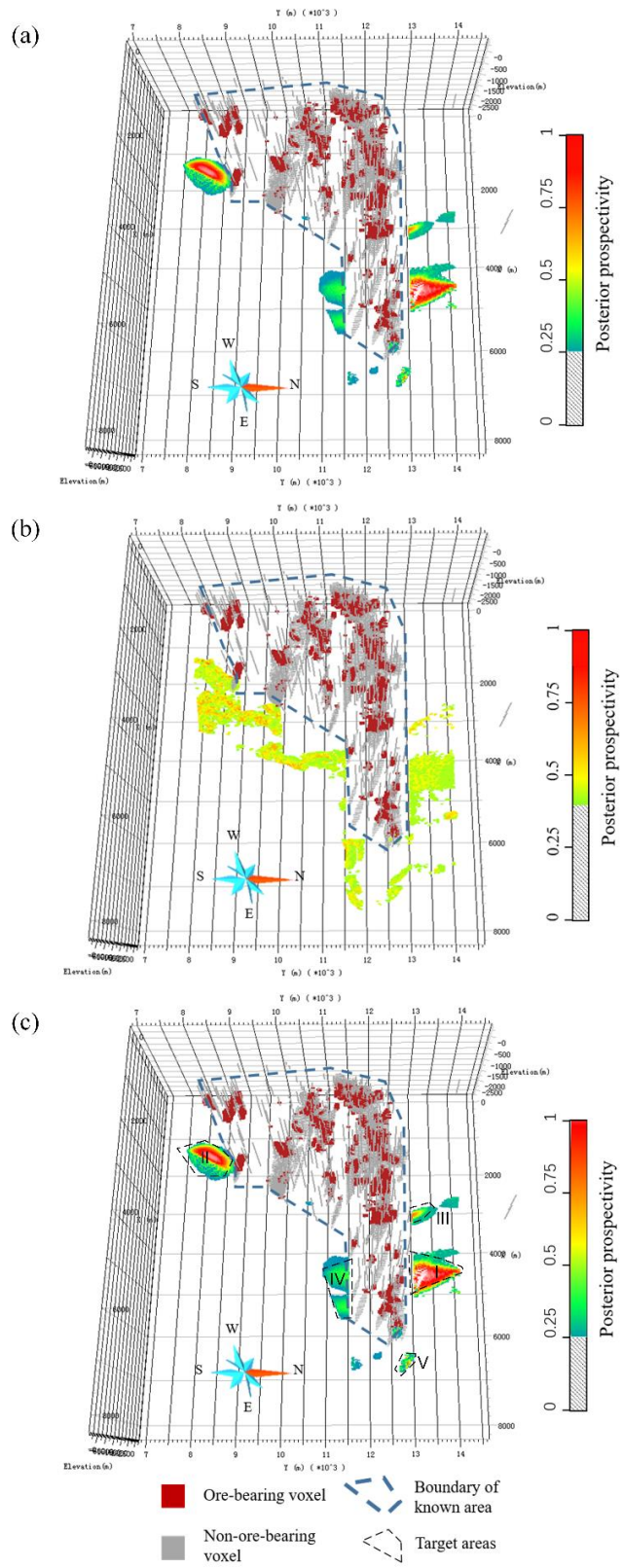


Figure 13: The Predictive results of the prospectivity models using (a) CNN, (b) random forests and (c) the exploration targets resulting from CNN model.

Table 2: MYIs and the corresponding probabilities for the prospective models based on the CNN and the random forest.

Prospectivity model	MYI	Probability
CNN	0.801	0.253
Random forest	0.569	0.394

5. Conclusions

This paper proposes a 3D MPM method with CNNs, in which the 3D mineral prospectivity is directly learn from 3D geological models. As demonstrated in a case study from gold prospecting in Dayingezhuang gold deposit, the proposed method shows several advantages compared with the conventional machine learning-based methods for 3D MPM. Firstly, by reorganizing the geometry of the unstructured 3D geological models into deep networks, the proposed method is capable of exploiting the deep network architecture to capture and reason complex correlation between the geometry of the geological boundary to the localization of mineralization. This allows to boost the performance of 3D MPM in both prediction accuracy and targeting efficiency. Secondly, attributed to the representation learning ability of CNNs, the method can automatically disentangle underlying factors to mineralization and learn prospectivity-informative representation for 3D MPM. This opens a door to circumvent the tedious work for designing predictor variables in the conventional mineral prospectivity framework and provides an effective and efficient way to achieve 3D MPM. Thirdly, since the 2D CNNs enable us to repurpose the mature 2D CNN architecture and to pre-train on the available image dataset, we can train and construct a 3D prospectivity model in an efficient and simple way with the exploration data at deposit-scale. Last but not least, by learning mineral prospectivity from the geometry of 3D geological models, our prospectivity model can be more objective and faithful to the massive training set and provide deeper insight for exploration targeting, which permits us to prevent the impact of subjective understanding and limitation in prior knowledge and conceptual models. Therefore, these advantages make the proposed method be a novel but more powerful tool ensuring lower work-load and prospecting risk in prediction of deep-seated concealed orebodies.

There are still some limitations in our method and several interesting directions for future work. Despite the CNN-based model achieves promising performance, our method only learns mineral prospectivity from a single geological

model owing to the special geological setting in the study area. The proposed network architecture is required to be expanded for adapting the scenario of multiple ore-controlling geological boundaries. However, it is straightforward to expand the proposed network architecture by reusing the proposed network to learn from each geological model and aggregating the high-level representations of each geological model for mineral prospectivity. In the future, we will search for a deposit of more ore-controlling geological boundaries and carry out 3D MPM with the expanded network. In addition, the interpretability of the CNN-based model is another concern. This drives us to open the black box of the model and make the model more transparent to geologists in the future.

Acknowledgments

This study is partially supported by National Natural Science Foundation of China (Nos. 41972309, 42030809, and 42072325) and National Key Research and Development Program of China (No. 2017YFC0601503).

Code availability section

3DMPM

Contact: chengyann1222@gmail.com

Hardware requirements: GeForce RTX 1050Ti or higher.

Program language: MATLAB, C++ and Python.

Software required: MATLAB2020b, Visual Studio, Ubuntu 18.04 and Anaconda.

Program size: 9.67 MB.

The source codes are available for downloading at the link:

<https://github.com/ChengYeung1222/3DMPM>

References

- Abadi, M., Barham, P., Chen, J., Chen, Z., Davis, A., Dean, J., Matthieu D., Sanjay G., Geoffrey I., Michael I., Manjunath K., Josh L., Rajat M., Sherry M., Derek G.M., Benoit S., Paul T., Vijay V., Pete W., Martin W., Yuan Y., Zheng, X., 2016. Tensorflow: A system for large-scale machine learning. In 12th Advanced Computing Systems Organization symposium on operating systems design and implementation ({OSDI} 16), pp. 265-283.
- Agterberg, F.P., Bonham-Carter, G.F., 2005. Measuring the performance of mineral-potential maps. *Natural Resources Research*, 14(1), 1-17.
- Agterberg, F.P., Bonham-Carter, G.F., Cheng, Q. M., Wright, D. F., 1993. Weights of evidence modeling and weighted logistic regression for mineral potential mapping. *Computers in geology*, 25, 13-32.
- Bai, S., Lü, G., Wang, J., Zhou, P., Ding, L., 2011. GIS-based rare events logistic regression for landslide-susceptibility mapping of Lianyungang, China. *Environmental Earth Sciences*, 62(1), 139-149.
- Barreno, M., Cardenas, A., Tygar, J. D., 2007. Optimal ROC curve for a combination of classifiers. *Advances in Neural Information Processing Systems*, 20, 57-64.
- Baykan, N.A., Yilmaz, N., 2011. A mineral classification system with multiple artificial neural network using k-fold cross validation. *Mathematical and Computational Applications*, 16(1), 22-30.
- Cao, W., Liu, L., Liu, H., Lai, F., 2020. Investigating the Irregular Localization of Skarn Orebodies by Computational Modeling in the Fenghuangshan Ore Field, Tongling District, Anhui Province, China. *Natural Resources Research*, 1-22.
- Carranza, E.J.M., 2011. Analysis and mapping of geochemical anomalies using logratio-transformed stream sediment data with censored values. *Journal of Geochemical Exploration*, 110(2), 167-185. Carranza, E. J. M., 2011. Geocomputation of mineral exploration targets. *Computers & Geosciences*, 37(12), 1907-1916.
- Deng, J., Dong, W., Socher, R., Li, L.J., Li, F.F., 2009. ImageNet: a Large-Scale Hierarchical Image Database. 2009 IEEE Computer Society Conference on Computer Vision and Pattern Recognition (CVPR 2009), 20-25 June 2009, Miami, Florida, USA. IEEE.
- Deng, J., Yang, L.Q., Groves, D.I., Zhang, L., Qiu, K.F., Wang, Q.F., 2020. An integrated mineral system model for the gold deposits of the giant Jiaodong province, eastern China. *Earth-Science Reviews*, 103274.

- Donahue, J., Jia, Y., Vinyals, O., Hoffman, J., Zhang, N., Tzeng, E., Darrell, T., 2014, January. Decaf: A deep convolutional activation feature for generic visual recognition. In International conference on machine learning, pp. 647-655.
- Esteva, A., Kuprel, B., Novoa, R. A., Ko, J., Swetter, S.M., Blau, H.M., Thrun, S., 2017. Dermatologist-level classification of skin cancer with deep neural networks. *Nature*, 542(7639), 115-118.
- Gao, Y., Zhang, Z., Xiong, Y., Zuo, R., 2016. Mapping mineral prospectivity for Cu polymetallic mineralization in southwest Fujian Province, China. *Ore Geology Reviews*, 75, 16-28.
- Goldfarb, R.J., Santosh, M., 2014. The dilemma of the Jiaodong gold deposits: are they unique? *Geoscience Frontiers*, 5(2), 139-153.
- He, K., Zhang, X., Ren, S., Sun, J., 2015. Delving deep into rectifiers: Surpassing human-level performance on imagenet classification. In Proceedings of the IEEE international conference on computer vision, pp. 1026-1034.
- Nair, V., Hinton, G. E., 2010. Rectified linear units improve restricted boltzmann machines. International Conference on International Conference on Machine Learning, pp. 807- 814.
- Hinton, G.E., Srivastava, N., Krizhevsky, A., Sutskever, I., Salakhutdinov, R.R., 2012. Improving neural networks by preventing co-adaptation of feature detectors. arXiv preprint arXiv:1207.0580.
- Hu, X., Li, X., Yuan, F., Ord, A., Jowitt, S. M., Li, Y., Dai, W., Zhou, T., 2020. Numerical modeling of ore-forming processes within the Chating Cu-Au porphyry-type deposit, China: Implications for the longevity of hydrothermal systems and potential uses in mineral exploration. *Ore Geology Reviews*, 116, 103230.
- Hu, X., Yuan, F., Li, X., Jowitt, S. M., Jia, C., Zhang, M., Zhou, T., 2018. 3D characteristic analysis-based targeting of concealed Kiruna-type Fe oxide-apatite mineralization within the Yangzhuang deposit of the Zhonggu orefield, southern Ningwu volcanic basin, middle-lower Yangtze River metallogenic Belt, China. *Ore Geology Reviews*, 92, 240-256.
- Jean, N., Burke, M., Xie, M., Davis, W. M., Lobell, D. B., Ermon, S., 2016. Combining satellite imagery and machine learning to predict poverty. *Science*, 353(6301), 790-794.
- Jin, X., Wang, G., Tang, P., Hu, C., Liu, Y., Zhang, S., 2020. 3D geological modelling and uncertainty analysis for 3D targeting in Shanggong gold deposit (China. *Journal of Geochemical Exploration*, 210, 106442).
- Kalogerakis, E., Averkiou, M., Maji, S., Chaudhuri, S., 2017. 3D shape segmentation with projective convolutional networks. In proceedings of the IEEE conference on computer vision and pattern recognition, pp. 3779-3788.

- Krizhevsky, A., Sutskever, I., Hinton, G., 2012. ImageNet Classification with Deep Convolutional Neural Networks. *Advances in neural information processing systems*, 25, 1097-1105.
- Kumar, U., Raja, S.K., Mukhopadhyay, C., Ramachandra, T.V., 2011, January. A multi-layer perceptron based non-linear mixture model to estimate class abundance from mixed pixels. In *IEEE Technology Students' Symposium*, pp. 148-153. IEEE.
- Kyne, R., Torremans, K., Güven, J., Doyle, R., Walsh, J., 2019. 3-D modeling of the lisheen and silvermines deposits, County Tipperary, Ireland: insights into structural controls on the formation of Irish Zn-Pb deposits. *Economic Geology*, 114(1), 93-116.
- LeCun, Y., Bengio, Y., Hinton, G., 2015. Deep learning. *Nature*, 521(7553), 436-444.
- Li, L., Santosh, M., Li, S.R., 2015. The 'Jiaodong type' gold deposits: characteristics, origin and prospecting. *Ore Geology Reviews*, 65, 589-611.
- Li, N., Bagas, L., Li, X., Xiao, K., Li, Y., Ying, L., Song, X., 2016. An improved buffer analysis technique for model-based 3D mineral potential mapping and its application. *Ore Geology Reviews*, 76, 94-107.
- Li, T., Zuo, R., Xiong, Y., Peng, Y., 2020. Random-drop data augmentation of deep convolutional neural network for mineral prospectivity mapping. *Natural Resources Research*, 30(1), 27-38.
- Li, Y., 2015a. Three-dimensional mineral prospectivity modeling for targeting of concealed mineralization within the Zhonggu iron orefield, Ningwu Basin, China. *Ore Geology Reviews*, 71, 633-654.
- Lisle, R., 1994. Detection of Zones of Abnormal Strains in Structures Using Gaussian Curvature Analysis. *Aapg Bulletin - AAPG BULL.* 78. 1811-1819. 10.1306/A25FF305-171B-11D7-8645000102C1865D.
- Liu, L., Zhao, Y., Sun, T., 2012. 3D computational shape-and cooling process-modeling of magmatic intrusion and its implication for genesis and exploration of intrusion-related ore deposits: An example from the Yueshan intrusion in Anqing, China. *Tectonophysics*, 526, 110-123.
- Liu, Z., Hollings, P., Mao, X., Lawley, C.J., Yang, B., Tang, L., 2021a. Metal remobilization from country rocks into the Jiaodong-type orogenic gold systems, Eastern China: New constraints from scheelite and galena isotope results at the Xiadian and Majiayao gold deposits. *Ore Geology Reviews*, 104126.
- Liu, Z., Mao, X., Jedemann, A., Bayless, R. C., Deng, H., Chen, J., Xiao, K., 2021b. Evolution of Pyrite Compositions at the Sizhuang Gold Deposit, Jiaodong Peninsula, Eastern China: Implications for the Genesis of Jiaodong-Type Orogenic Gold Mineralization. *Minerals*, 11(4), 344.

- Macedo, I., Gois, J.P., Velho, L., 2011, March. Hermite radial basis functions implicit. In *Computer Graphics Forum*, Vol. 30, No. 1, pp. 27-42. Oxford, UK: Blackwell Publishing Ltd.
- Mao, X., Ren, J., Liu, Z., Chen, J., Tang, L., Deng, H., 2019. Three-dimensional prospectivity modeling of the Jiaojia-type gold deposit, Jiaodong Peninsula, Eastern China: A case study of the Dayingezhuang deposit. *Journal of Geochemical Exploration*, 203, 27-44.
- Mao, X., Zhang, B., Deng, H., Zou, Y., Chen, J., 2016. Three-dimensional morphological analysis method for geologic bodies and its parallel implementation. *Computers & Geosciences*, 96, 11-22.
- Maxmen, A., 2018. Deep learning sharpens views of cells and genes. *Nature*, 553(7686).
- Meyer, M., Desbrun, M., Schröder, P., Barr, A.H., 2003. Discrete differential-geometry operators for triangulated 2-manifolds. In *Visualization and mathematics III*, pp. 35-57. Springer, Berlin, Heidelberg.
- Nielsen, S.H., Cunningham, F., Hay, R., Partington, G., Stokes, M., 2015. 3D prospectivity modelling of orogenic gold in the Marymia Inlier, Western Australia. *Ore Geology Reviews*, 71, 578-591.
- Ord, A., Hobbs, B.E., Zhang, Y., Broadbent, G.C., Brown, M., Willetts, G., Zhao, C. 2002. Geodynamic modelling of the century deposit, Mt Isa Province, Queensland. *Australian Journal of Earth Sciences*, 49(6), 1011-1039.
- Porwal, A., Carranza, E.J.M., 2015. Introduction to the Special Issue: GIS-based mineral potential modelling and geological data analyses for mineral exploration.
- Ruopp, M.D., Perkins, N.J., Whitcomb, B.W., Schisterman, E.F., 2008. Youden Index and optimal cut-point estimated from observations affected by a lower limit of detection. *Biometrical Journal: Journal of Mathematical Methods in Biosciences*, 50(3), 419-430.
- Shabankareh, M., Hezarkhani, A., 2016. Application of support vector machines for copper potential mapping in Kerman region, Iran. *Journal of African Earth Sciences*, 128, 116-126.
- Silver, D., Huang, A., Maddison, C.J., Guez, A., Sifre, L., Van Den Driessche, G., Hassabis, D., 2016. Mastering the game of Go with deep neural networks and tree search. *Nature*, 529(7587), 484-489.
- Snow, D.T., 1969. Anisotropic permeability of fractured media. *Water resources research*, 5(6), 1273-1289.
- Srivastava, N., Hinton, G., Krizhevsky, A., Sutskever, I., Salakhutdinov, R., 2014. Dropout: a simple way to prevent neural networks from overfitting. *Journal of Machine Learning Research*, 15(1), 1929-1958.
- Taubin, G., 1995, September. A signal processing approach to fair surface design. In *Proceedings of the 22nd annual conference on Computer graphics and interactive techniques*, pp. 351-358.

- Wang, G., Li, R., Carranza, E.J.M., Zhang, S., Yan, C., Zhu, Y., Qu, J., Hong, D., Song, Y., Han, J., Ma, Z., Zhang H., Yang, F., 2015. 3D geological modeling for prediction of subsurface Mo targets in the Luanchuan district, China. *Ore Geology Reviews*, 71, 592-610.
- Wang, G., Zhang, S., Yan, C., Song, Y., Sun, Y., Li, D., Xu, F., 2011. Mineral potential targeting and resource assessment based on 3D geological modeling in Luanchuan region, China. *Computers & Geosciences*, 37(12), 1976-1988.
- Wang, S.R., Yang, L.Q., Wang, J.G., Wang, E.J., Xu, Y.L., 2019. Geostatistical determination of ore shoot plunge and structural control of the Sizhuang world-class epizonal orogenic gold deposit, Jiaodong Peninsula, China. *Minerals*, 9(4), 214.
- Wilson, C.J., Osborne, D.J., Robinson, J.A., Miller, J.M., 2016. Structural constraints and localization of gold mineralization in Leather Jacket Lodes, Ballarat, Victoria, Australia. *Economic Geology*, 111(5), 1073-1098.
- Xiao, K., Li, N., Porwal, A., Holden, E.J., Bagas, L., Lu, Y., 2015. GIS-based 3D prospectivity mapping: A case study of Jiama copper-polymetallic deposit in Tibet, China. *Ore Geology Reviews*, 71, 611-632.
- Xiong, Y., Zuo, R., 2018. GIS-based rare events logistic regression for mineral prospectivity mapping. *Computers & Geosciences*, 111, 18-25.
- Yang, L., Zhao, R., Wang, Q., Liu, X., Carranza, E.J.M., 2018. Fault geometry and fluid-rock reaction: combined controls on mineralization in the Xinli gold deposit, Jiaodong Peninsula, China. *Journal of Structural Geology*, 111, 14-26.
- Yang, L.Q., Deng, J., Goldfarb, R.J., Zhang, J., Gao, B.F., Wang, Z.L., 2014. $^{40}\text{Ar}/^{39}\text{Ar}$ geochronological constraints on the formation of the Dayingezhuang gold deposit: New implications for timing and duration of hydrothermal activity in the Jiaodong gold province, China. *Gondwana Research*, 25(4), 1469-1483.
- Yang, L.Q., Deng, J., Wang, Z.L., Guo, L.N., Li, R.H., Groves, D.I., ..., Zhao, H., 2016. Relationships between gold and pyrite at the Xincheng gold deposit, Jiaodong Peninsula, China: Implications for gold source and deposition in a brittle epizonal environment. *Economic Geology*, 111(1), 105-126.
- Zhang, B.L., Shan, W., Li, D.P., Xiao, B.J., Wang, Z.L., Zhang, R.Z., 2017. Hydrothermal alteration in the Dayingezhuang gold deposit, Jiaodong, China. *Acta Petrologica Sinica*, 33(7), 2256-2272.

- Zhang, D., Agterberg, F., Cheng, Q., Zuo, R., 2014. A comparison of modified fuzzy weights of evidence, fuzzy weights of evidence, and logistic regression for mapping mineral prospectivity. *Mathematical Geosciences*, 46(7), 869-885.
- Zhang, H., Van Kaick, O., Dyer, R., 2010, September. Spectral mesh processing. In *Computer graphics forum* (Vol. 29, No. 6, pp. 1865-1894). Oxford, UK: Blackwell Publishing Ltd.
- Zhang, S., Carranza, E.J.M., Wei, H., Xiao, K., Yang, F., Chen, Z., Li, N., Xiang, J., 2021. Data-driven Mineral Prospectivity Mapping by Joint Application of Unsupervised Convolutional Auto-encoder Network and Supervised Convolutional Neural Network. *Natural Resources Research*, 30(2), 1011-1031.
- Zhao, C., Hobbs, B.E., Ord, A., 2008. *Convective and advective heat transfer in geological systems*. Springer Science & Business Media.
- Zuo, R., Carranza, E.J.M., 2011. Support vector machine: a tool for mapping mineral prospectivity. *Computers & Geosciences*, 37(12), 1967-1975.
- Zuo, R., Xiong, Y., 2018. Big data analytics of identifying geochemical anomalies supported by machine learning methods. *Natural Resources Research*, 27(1), 5-13.
- Zuo, R., Xiong, Y., Wang, J., Carranza, E.J.M., 2019. Deep learning and its application in geochemical mapping. *Earth-science reviews*, 192, 1-14.

List of Figures

1. Figure 1: 3D MPM pipeline and architecture that use the 2D CNN to learn from the 3D geological model.
2. Figure 2: Laplacian operator.
3. Figure 3: The iteration process in optimization of the viewing direction: the projected areas (left column) and the projected images illustrating the distance to the target voxel (right column) at (a) 1st, (b) 3rd, (c) 4th and (d) 11th iterations are presented. Note that the projected areas gradually converge to the zone that is more close to the target voxel as the result of maximization of Equation (7).
4. Figure 4: The AlexNet-based CNN architecture for prospectivity modeling.
5. Figure 5: Geological map of the Dayingezhuang gold deposit (after Mao et al., 2019).
6. Figure 6: The mineralization-alteration zoning pattern (at section line #86) of the Dayingezhuang gold deposit.
7. Figure 7: Known voxels (Au grade >1g/t) (a), 3D mesh models of the Zhaoping fault (b) and orebodies (c).
8. Figure 8: Shape descriptors of (a) eigenfunctions and (b) surface normals of Zhaoping fault, Dayingezhuang segment.
9. Figure 9: Projection results of shape descriptors: (a) eigenfunctions and (b) surface normals of Zhaoping fault, Dayingezhuang segment (at one location, Size: 227x227).
10. Figure 10: The training procedure for prospectivity modeling (a) accuracy and (b) cross-entropy at different epochs.
11. Figure 11: Fuzziness of predicted posterior probability at different epochs.
12. Figure 12: ROC curves (a) and capture-efficiency curves (b) of five evaluated prospectivity models.
13. Figure 13: The Predictive results of the prospectivity models using (a) CNN, (b) random forests and (c) the exploration targets resulting from CNN model.

List of Tables

1. Table 1: Targeting criteria, predictor variables and corresponding spatial analysis approach for 3D MPM in Dayingezhuang deposit.
2. Table 2: MYIs and the corresponding probabilities for the prospective models based on the CNN and the random forest.